Received 18 June 2025; Accepted 22 September 2025
https://doi.org/10.48612/letters/2025-4-236-248
https://elibrary.ru/neltyd

Enhanced mechanical properties and corrosion resistance synergy of multi-layered aluminum sheets fabricated with interlayer

Z. Yuan[1], Y. Lu[1], Y. Jiang[1], X. Wang[†1], Z. Ni[1], Y. Tu[2], J. Peng[1],
Z. Liu[3], Q. Zhang[4], P. Wang[5], Y. Peng[6]

[†]wangxingxing@ncwu.edu.cn

[1]School of Materials Science and Engineering, North China University of Water Resources and Electric Power, Zhengzhou 450040, China
[2]School of Materials Science and Engineering, Southeast University, Nanjing 211189, China
[3]College of Materials Science and Technology, Nanjing University of Aeronautics and Astronautics, Nanjing 210016, China
[4]Jiangsu Alcha Aluminium Group Co., Ltd., Changshu 215500, China
[5]Henan Key Laboratory of High Performance Carbon Fiber Reinforced Composites, Institute of Carbon Matrix Composites, Henan Academy of Sciences, Zhengzhou 450046, China
[6]CITIC Heavy Industries Co. Ltd., Luoyang 471039, China

Abstract: This study systematically investigates the dual enhancement of mechanical properties and corrosion resistance in multi-layered aluminum sheets achieved through the introduction of an interlayer. The interlayer serves as an effective diffusion barrier during the brazing process, significantly impeding the inward migration of Si atoms from the clad layer into the AA3xxx core. This mitigation of Si diffusion not only preserves the microstructural integrity of the core layer but also reduces the risk of intergranular corrosion. Furthermore, natural aging promotes the precipitation of Guinier–Preston (GP) zones within the core matrix, contributing substantially to yield strength improvement through coherent precipitation hardening. First-principles calculations based on the density functional theory were employed to analyze the relatively stable atomic structure and the bonding mechanism of GP zones. The maximum in work of adhesion (W_{ad}) appears in the Al(010)/MgSi(010) B-C interface. The strength of bond between Al and Si atoms in the Al(010)/MgSi(010) interface is stronger than that in Al(010)/Al_2MgSi(001) and Al(010)/Al_6MgSi(001) interfaces. Additionally, electronic structure and work function analyses demonstrated that the potential difference between the GP zones and the surrounding Al matrix is minimal, thereby suppressing micro-galvanic corrosion. As a result, the multi-layered aluminum sheets exhibit significant enhancements in both mechanical strength and corrosion resistance.

Keywords: multi-layered aluminum sheet, GP zones, first-principles, natural aging, mechanical properties

Acknowledgments: *This research was financially supported by the National Natural Science Foundation of China (52475347), and the Program for Science & Technology Innovation Talents in Universities of Henan Province (24HASTIT045). Project was sponsored by the Key Research and Development Projects in Henan Province (251111222600), the Key Scientific Research Projects in Higher Education Institutions in Henan Province (25A430030) and Scientific and Technological Key Project in Henan Province (252102231035).*

1. Introduction

New energy vehicles (NEVs) represent a critical shift toward addressing climate change and advancing sustainable development. Within NEVs, power batteries function as the core component, with ongoing improvements to maximize specific capacity, efficiency, and safety in sheets play a vital role in the construction of heat exchangers for these power batteries [1]. Typically, a layered aluminum structure is used, where an AA3xxx (Al-Mn) alloy core layer is clad with an AA4xxx (Al-Si) alloy [2, 3]. This cladding design facilitates efficient heat exchanger connections. And the core ensures its required structural strength. The clad alloy, containing around 10% Si, lowers the melting point of the composite and forms an even covering on each side of the core layer.

In recent studies, AA3xxx alloys have been strengthened through alloying additions [4]. Incorporating copper and magnesium has shown measurable improvements in the yield strength: Cu raises the yield strength to 40 – 60 MPa post-brazing, while Mg additions further enhance strength by promoting the nano-precipitate formation during natural aging [5]. Schmatz et al. [6] have shown that during brazing, the clad alloy contains Cu which diffuses from the core alloy, while Si migrates inward. This migration reduces the ability to provide sacrificial protection of the clad alloy, thereby reducing its overall corrosion resistance. Si elements diffused from the clad layer along grain boundaries promote micro-

galvanic interactions at Si particles/Al matrix interface, often leading to intergranular corrosion (IGC) [7].

Afshar et al. [8–10] found that α-Al(Fe,Mn)Si particles within 5 μm of the surface in AA4xxx/AA3xxx sheets can form galvanic coupling with internal layers, accelerating dissolution and intergranular corrosion. Removing such sites may enhance corrosion resistance. Recent studies show that adding an interlayer between the AA4xxx and AA3xxx alloys improves air-side corrosion protection [11] by acting as a sacrificial layer and extending Si and Cu diffusion paths, which helps prevent the Cu-rich intermetallic formation. Shi et al. [12] established cross-sectional corrosion potential profiles for a multilayer aluminum brazing sheet (AA4045/7072/3003/4045), showing that the interlayer functioned as a buffer, inhibiting Si diffusion from the clad to core while restricting outward Cu migration. This interlayer effectively reinforces corrosion resistance while preserving the integrity of the AA3xxx core.

This study builds on these insightful investigating the influence of an interlayer in both mechanical strength and corrosion resistance. By acting as a diffusion barrier, this interlayer significantly slows down the Si penetration into the core during brazing, extending lifespan of the material against corrosion. Additionally, incorporating Mg into the core alloy could allow for limited precipitation hardening, which may further enhance the strength. Both high-resolution transmission electron microscopy (HRTEM) and scanning electron microscopy (SEM) enables a comprehensive microstructural analysis of these alloy layers, offering a detailed understanding of how interlayer modifications can optimize both strength and corrosion resistance.

2. Experimental

2.1. Materials

Four-layered Al sheets AA4343/AA3xxx/AA3xxx/AA4343 are studied as experimental materials. The core layer consisted of an AA3xxx alloy, with a 32 μm AA3xxx interlayer on top and a 27 μm layer of AA4343 below it. A layer of a 14 μm thick AA4343 material is placed on the 32 μm thick AA3xxx interlayer. The clad, interlayer and core alloys are melted with a vacuum melting furnace (SJF14Q). An Inductively Coupled Plasma Optical Emission Spectrometry (ICP-OES) analyzer is utilized to determine the content of the four-layered Al sheets, and Table 1 shows their composition. Figure 1 shows the preparation process of the experimental materials. The assembled materials were preheated at 490°C for 8 h followed by hot roll bonding to a thickness of 2.8 mm. Afterward, intermediate annealing was conducted at 460°C for 13 hours, and then air-cooled to room temperature. Then these sheets obtained by the above steps are cold-rolled, and the thickness is kept at 0.28 mm. The samples were placed in controlled atmosphere brazing furnace for simulated brazing. The materials were heated up to 600°C (at 30°C/min), and were held at that temperature for 5 min and then cooled down at a specified rate of 60°C/min.

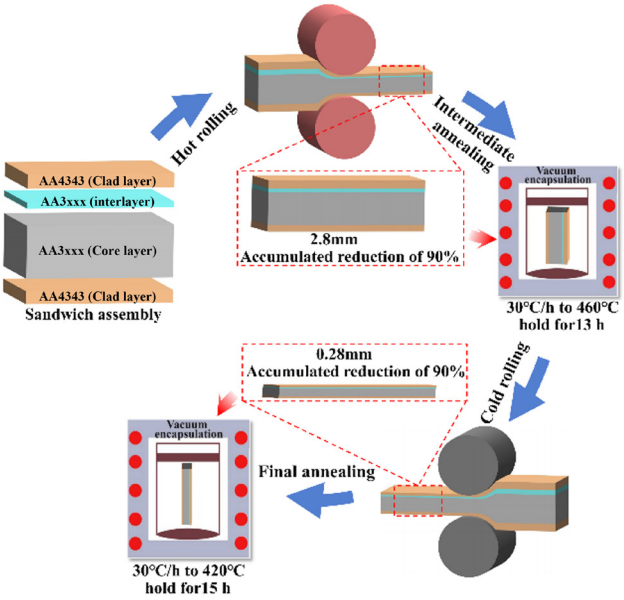

Fig. 1. (Color online) Fabrication of AA4343/AA3xxx/AA3xxx/AA4343 multi-layer aluminum sheets.

2.2. Microstructure characterization

SEM was utilized to confirm the particle composition and morphology. Glow discharge optical emission spectrometry (GDOES) provided quantitative line scans of Cu, Fe, Mn, and Si elements throughout the cross-sections of the aluminum sheet before and after brazing. With the voltage (15–18 V), a double-jet electro-polishing device was employed to prepare the thin films for Transmission electron microscope (TEM) observation. The precise crystal structure and microstructure of the nano-precipitated phases were explored using HRTEM (Tecnai F30) with the assistance of bright field (BF) and a selected area diffraction pattern (SADP).

2.3. Calculation methods

In this work, the interfacial properties, surfaces, and crystal structures were confirmed by simulations with CASTEP (Cambridge Sequential Total Energy Package) code [13,14]. Ultrasoft pseudopotential method can precisely describe the mutual influence among various ionic cores and valence electrons. The SCF (Self-Consistent Field) method, an approximate approach was chosen for calculating the total

Table 1. Chemical composition (wt.%) and thickness of the brazing sheets.

Alloy	Layer	Thickness	Si	Fe	Cu	Mn	Mg	Zn	Zr	Ti	Al
AA4343	Clad	14 μm	7.8	0.26	0.06	0.08	-	0.02	0.06	0.16	Bal.
AA3xxx	Interlayer	32 μm	0.89	0.26	0.08	1.82	-	2.78	-	0.03	Bal.
AA3xxx	Core	207 μm	0.79	0.35	0.38	0.66	0.27	0.02	-	0.13	Bal.
AA4343	Clad	27 μm	7.8	0.26	0.06	0.08	-	0.02	0.06	0.16	Bal.

energy of the interfaces, especially in complex multi-particle situations due to the Schrödinger equation. To study the electron exchange correlation, the Perdew-Burke-Ernzerhof (PBE) form of the generalized gradient approximation (GGA) was employed in geometry optimization of the crystal structures [15,16].

To achieve accurate computational results while optimizing resource efficiency, convergence tests were performed on the cut-off energy and k-point mesh. A 6×6×6 k-point mesh was set for Al, MgSi, and Al_2MgSi crystals to calculate their total energy, and Al_6MgSi is calculated with a k-point mesh of 6×6×3. And 6×6×1 mesh was applied for surface and interface structure calculations. A 400 eV cutoff energy was applied in the plane wave method. Additionally, a convergence criterion of 1.0×10^{-5} eV/atom was established for total energy calculations. During maximal ionic displacement, a threshold of 0.001 Å was adequate to achieve convergence. For maximum stress, 0.05 GPa was considered moderate. A 0.03 eV/Å was set for the maximum ionic Hellmann-Feynman force.

The configuration and models of Al, MgSi, Al_2MgSi, and Al_6MgSi are displayed in Fig. 2. It is important to note that the construction of these lattices relies on the nano-precipitated phase (GP Zones) formed within the multilayered aluminum sheets. They all have clear Fm-3m space groups. With the PBE exchange-correlation functional, optimized MgSi, Al_2MgSi, and Al_6MgSi crystal cells were obtained. Table 2 reveals the difference of lattice constants after relaxation. These parameters indicate that the results in this work are close to other works. Therefore, these parameters are representative and precise in the calculation. When the number of Al layers is 0, 1, and 3 among organized Mg/Si(010) layers, the three structural models are ascertained. Consistent with the previous experiment, the lattices of three GP crystals are completely congruent with Al matrix.

Table 2. Difference of MgSi, Al_2MgSi, and Al_6MgSi lattice parameters in this work and others.

Structure	Source	Lattice constants (Å)		
		a	*b*	*c*
MgSi	This work	4.17	-	4.01
	Calculation [17]	4.23	-	3.92
	Calculation [18]	4.21	-	3.96
	Experiment [19]	4.05	4.05	4.05
Al_2MgSi	This work	3.95	-	3.95
	Calculation [17]	4.01	-	4.25
	Calculation [18]	4.00	-	4.28
	Experiment [19]	4.05	4.05	4.05
Al_6MgSi	This work	4.03	-	8.22
	Calculation [17]	4.00	-	8.36
	Calculation [18]	4.03	-	8.29
	Experiment [19]	4.05	4.05	8.10

To mitigate the influence of crystal periodicity in the calculations, a 15 Å vacuum layer was introduced. This layer was positioned at the top of the structure. In Fig. 3, Al(010) surfaces are stacked in "ABAB" sequence. The MgSi(010) surface has the regularity of stacking 'CDCD'. For concise expression, the outermost layers containing Al atom were defined as layer "A". The outermost layers containing Si atoms were defined as layer "C". And the interface is viewed as "A-C". Figure 3 shows a top perspective of the Al atom layer structure at this interface.

The calculation of work functions for adsorbed surfaces holds greater practical relevance than idealized "pristine surface" models, as metallic alloys inevitably interact with environmental species under operational conditions. Specifically, spontaneous adsorption of O or Cl atoms occurs when materials are exposed to atmospheric or aqueous environments, critically influencing corrosion behaviors. To systematically investigate these mechanisms, we constructed slab models representing four characteristic surfaces: Al(111), MgSi 010), Al_2MgSi(111), and Al_6MgSi(010). O and Cl atoms were adsorbed at top sites of distinct surface atoms (Fig. 4), enabling the simulation of work function modifications corresponding to two aggressive environments: (1) oxide-dominated degradation in humid air and (2) chloride-induced corrosion in marine settings. This approach quantitatively links electronic structure modulation to macroscopic corrosion resistance through the calculation of work function.

2.4. Mechanical properties

Tensile specimens with a length of 50 mm were machined to follow the guidelines of the ASTM E8/E8M-16a [20]. The tests were performed using MTS810 at RT. Drawing direction is the rolling direction, and the average rate is 1mm/min. Three samples were subjected to testing for each condition, and the resulting data were averaged to obtain the final values.

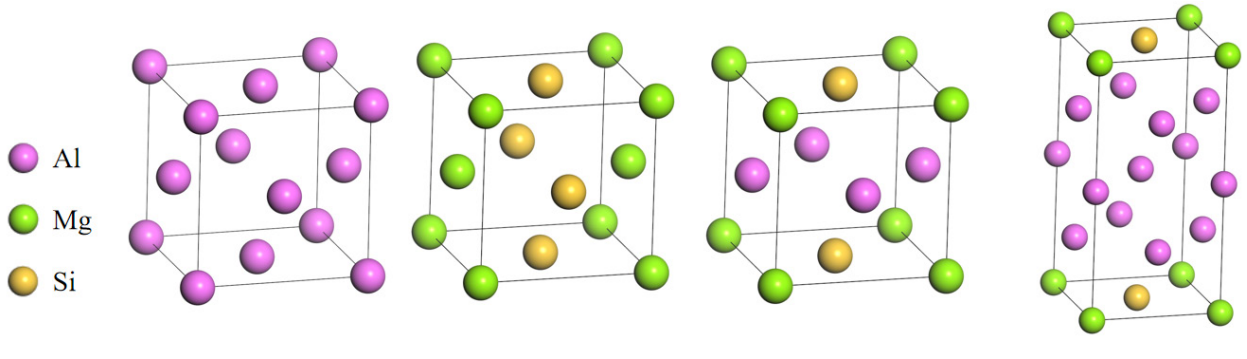

Fig. 2. (Color online) The crystal structures of Al (a), MgSi (b), Al_2MgSi (c), and Al_6MgSi (d).

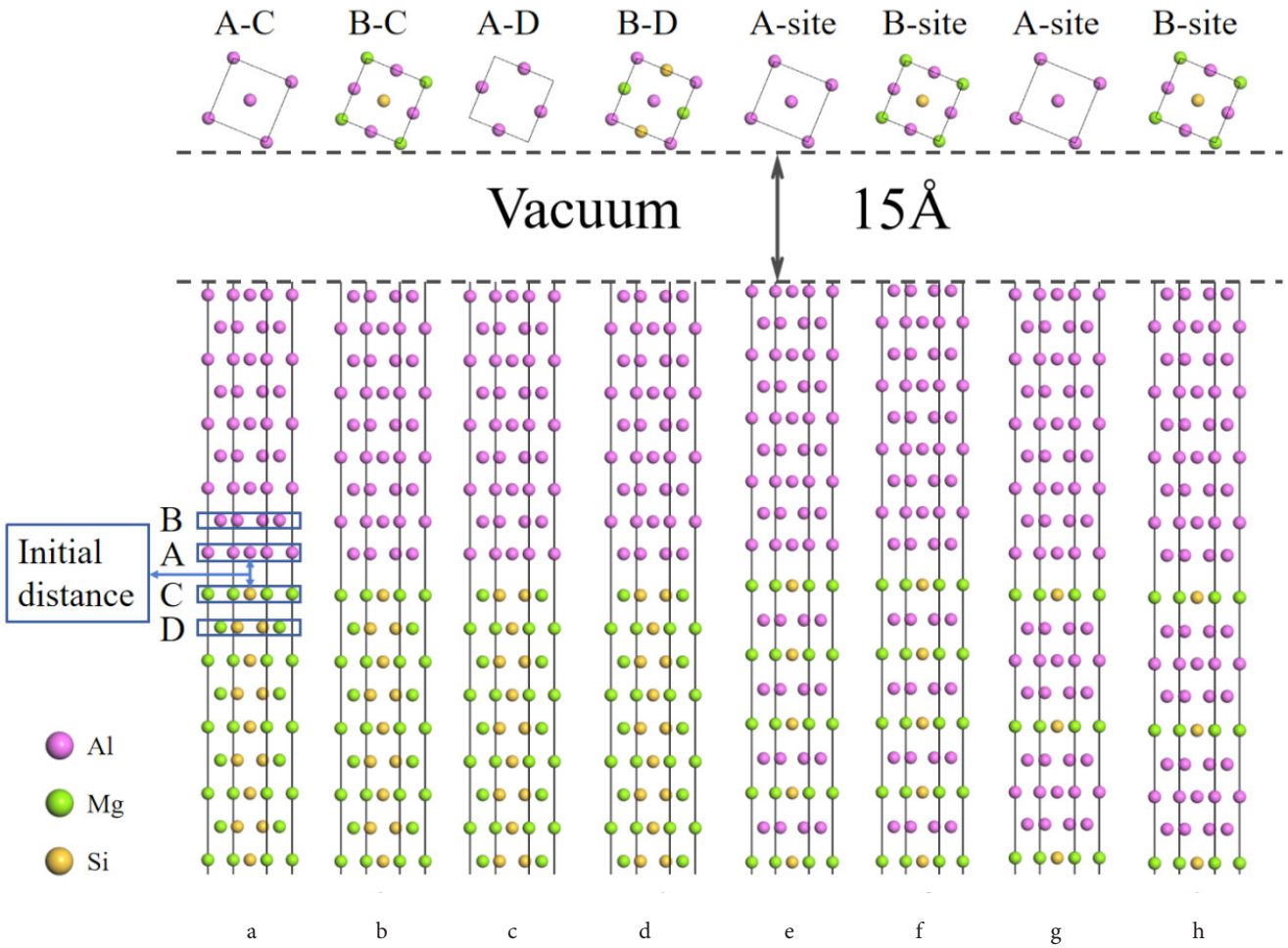

Fig. 3. (Color online) Interface models of Al(010)/MgSi(010) interface: A-C site (a), B-C site (b), A-D site (c), B-D site (d), Al(010)/Al_2MgSi(010) interface: A-site (e), B-site (f), and Al(010)/Al_6MgSi(001) interface: A-site (g), B-site (h).

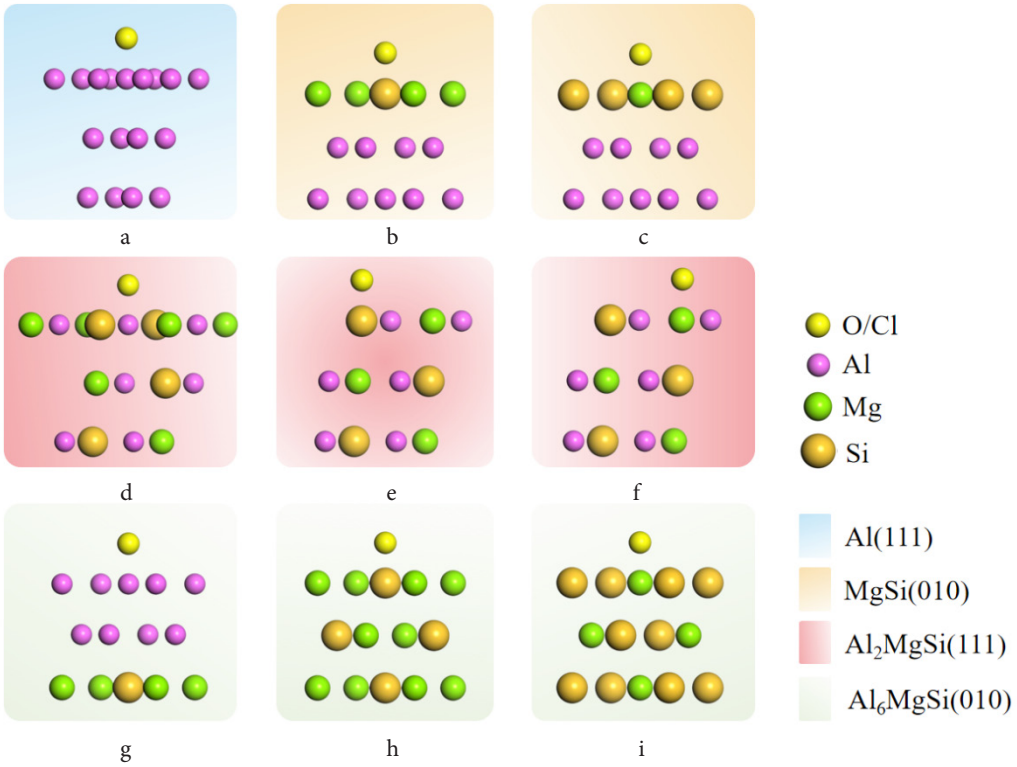

Fig. 4. (Color online) Adsorption Models of Al(010) (a), MgSi(010) (b – c), Al_2MgSi(111) (d – f), and Al_6MgSi(010) (g – i).

2.5. Corrosion attack mechanism

The corrosion resistance of these sheets was measured using the Salt Water Acetic Acid Test (SWAAT), the most commonly applied test way for this purpose [21]. A tape, 3 M Scotch brand M470, was utilized to protect the edges and back side [22]. A 3.5 wt.% NaCl solution, acidified with glacial acetic acid and adjusted to a pH of 2.8 using a 10 wt.% NaOH solution was applied as the corrosive spray. The corrosion attack mechanism was elucidated by observing the surface of the sheets post-SWAAT exposure using SEM.

3. Results

3.1. Microstructural analyses

3.1.1. Multi-layered aluminum sheets cross-sectional analyses

Sheet cross-sectional microstructures and EDS mapping results are illustrated in Fig. 5. The four-layer sheet interface is clearly visible before brazing process. This phenomenon is attributed to the difference in composition. The cladding layer includes α-Al matrix and Si particles. The interlayer and core layer are composed of many Fe/Mn-rich particles. During brazing, many Al-Si eutectic crystals appeared on the grain boundary and resolidified cladding layer surface, and a number of Mn intermetallic compounds precipitated within the interlayer.

3.1.2. Elemental depth profiling

In Fig. 6, GDOES reveals the element distribution in the sample that varies with depth. Before brazing, the cladding

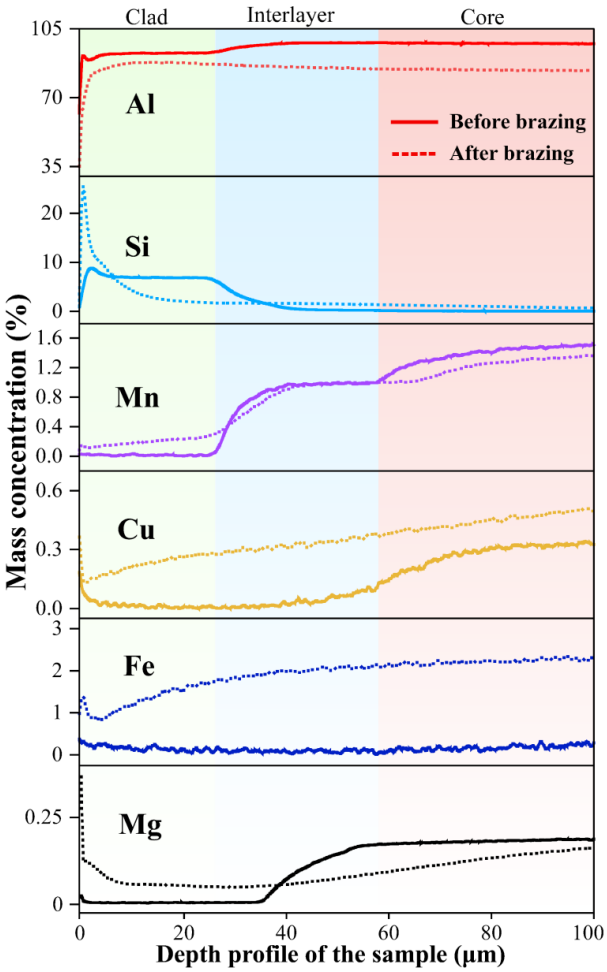

Fig. 6. (Color online) GDOES profiles of multi-layered Al sheets during whole brazing.

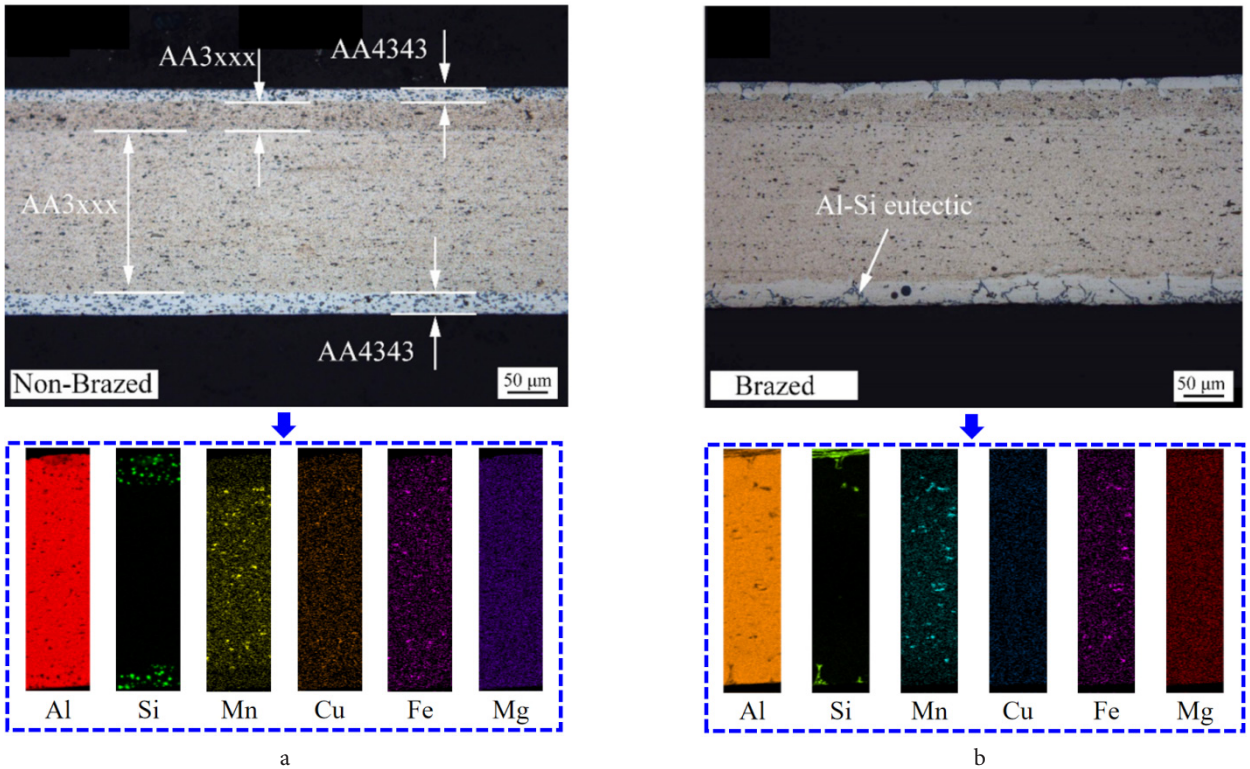

Fig. 5. (Color online) Microstructural images of multi-layered Al sheets: before brazing (a), after brazing (b).

alloy contained Si at a concentration of 8 wt.%. This can be seen from the solid lines, which indicate the distribution of elements before brazing. After brazing, re-solidified layer surface contains 0.25 wt.% Cu element. This can be seen from the dotted lines, which indicate the distribution of elements after brazing. It reveals Cu diffusion from the core alloy into re-solidified layer and interlayer. The interlayer separates the core from the clad layer which weakens Cu element diffusion in the core to the re-solidified layer. Additionally, the Si concentration shows a noticeable increase on the re-solidified clad layer surface (Fig. 6).

3.2. Calculation results

3.2.1. Work adhesion

The evaluation of interfacial bonding strength at a two-phase interface is often conducted using adhesive work. This directly expresses the energy, which is needed to separate two surfaces [23]. According to Eqs. (1), (2), and (3), we can calculate the W_{ad} of Al(010)/MgSi(010), Al(010)/Al_2MgSi (001), and Al(010)/Al_6MgSi (001) interfaces [24 – 26]:

$$W_{\text{ad-Al(010)/MgSi(010)}} = \left(E_{\text{Al(010)}} + E_{\text{MgSi(010)}} - E_{\text{Al(010)/MgSi(010)}}\right)\Big/A, \quad (1)$$

$$W_{\text{ad-Al(010)/Al}_2\text{MgSi(001)}} = \left(E_{\text{Al(010)}} + E_{\text{Al}_2\text{MgSi(001)}} - E_{\text{Al(010)/Al}_2\text{MgSi(001)}}\right)\Big/A, \quad (2)$$

$$W_{\text{ad-Al(010)/Al}_6\text{MgSi(001)}} = \left(E_{\text{Al(010)}} + E_{\text{Al}_6\text{MgSi(001)}} - E_{\text{Al(010)/Al}_6\text{MgSi(001)}}\right)\Big/A. \quad (3)$$

In these equations, $E_{Al(010)}$, $E_{MgSi(010)}$, $E_{Al_2MgSi(001)}$, and $E_{Al_6MgSi(001)}$ are the energy of foregoing surface when Al(010), MgSi(010), Al_2MgSi(001), and Al_6MgSi(001) surface all have nine atomic layers. $E_{Al(010)/MgSi(010)}$, $E_{Al(010)/Al_2MgSi(001)}$, and $E_{Al(010)/Al_6MgSi(001)}$ represent the total energy of Al(010)/MgSi(010), Al(010)/Al_2MgSi(001), and Al(010)/Al_6MgSi(001) interface. "A" is the interface region.

Figure 7 shows the correlation between W_{ad} and the distance of interface. The ordering of W_{ad} values at the Al(010)/MgSi(010) interface after relaxation is: B-C(1.52 J/m^2)>A-D(1.41 J/m^2)>A-C(1.11 J/m^2)>B-D(1.05 J/m^2). The interfacial distance (d_0) at B-C interface is 2.19 Å, which is less than initial distance 2.40 Å. At A-D interface, it started at 2.2 Å and changed into 2.02 Å. At A-C interface this parameter decreased to 2.71 Å with original value 3.1 Å. The d_0 of B-D interface decreased from 3.1 Å to 2.77 Å. The ordering of W_{ad} values at the Al(010)/Al_2MgSi(001) interface after relaxation is: B-site(1.15 J/m^2) > A-site(1.06 J/m^2). At the B-site interface, this distance increased from 2.20 Å to 2.22 Å. Meanwhile, at the A-site interface, it reached 2.68 Å. The ordering of W_{ad} values at the Al(010)/Al_6MgSi(001) interface after relaxation is: B-site(1.24 J/m^2) > A-site(1.03 J/m^2). At B-site interface, interfacial distance exhibited a slight decline. It was kept at 2.14 Å from 2.2 Å. But at A-site interface, it could surge to 2.66 Å starting from 2.6 Å. There is a noticeable result about W_{ad}. Among these interfaces, W_{ad} of A-site is lower than the others. At the A-site, the Al atom has a slight movement above Mg and Si atoms. It may be the cause of higher W_{ad}.

Figure 7 reveals fundamental insights into the relationship between interfacial structure and adhesion strength. The consistently superior performance of hollow-site configurations (e.g., B-C at Al/MgSi interface) is attributed to the maximized coordination number and efficient charge redistribution, leading to strong atomic attraction evidenced by shortened interfacial distances (e.g., 2.19 Å). Conversely, top-site configurations (e.g., A-site across interfaces) exhibit weaker bonding due to geometric constraints that limit orbital overlap and cause electronic repulsion, resulting in larger equilibrium distances (≈2.7 Å). This mechanistic understanding explains the "loosely arranged" electronic structure at these sites. Furthermore, the general superiority of Al/MgSi interfaces over Al/Al_2MgSi and Al/Al_6MgSi systems stems from better crystallographic matching that minimizes misfit strain. These atomic-level insights provide a critical design principle: promoting hollow-site bonding during processing should enhance mechanical properties by creating interfaces more resistant to debonding and crack propagation.

The highest W_{ad} value is observed for the B-C stacking at the Al(010)/MgSi(010) interface. The significantly shortened interfacial distance indicates strong atomic attraction and orbital overlap. In this configuration, the adsorbate atom sits within a hollow site, maximizing its coordination number with the substrate atoms. This allows for the formation of multiple strong bonds, leading to efficient charge redistribution and a more stable, lower-energy interface, which is thermodynamically more favorable to form. It is observed at the B-C stacking site of the Al(010)/MgSi(010) interface directly implies enhanced mechanical performance of the composite material.

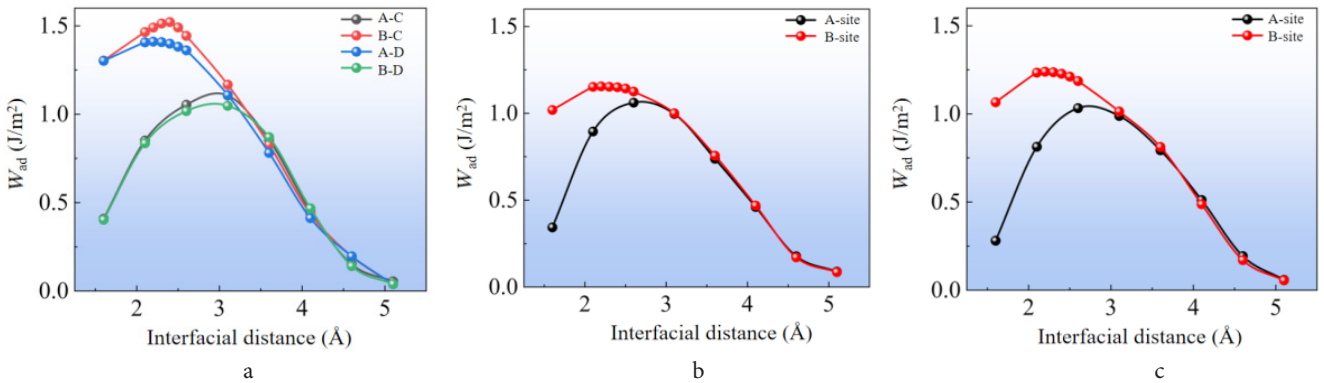

Fig. 7. (Color online) Relations between the interfacial distance and W_{ad}: Al(010)/MgSi(010) interface (a), Al(010)/Al_2MgSi(001) interface (b), and Al(010)/Al_6MgSi(001) interface (c).

3.2.2. Electronic structure

The spatial distribution of charge density is shown in Fig. 8 (a1, a2, a3). Atoms were sliced for intuitive analysis of charge density (b1, b2, b3) and differential charge density (c1, c2, c3). Between the Mg-Si and Al-Si atoms in MgSi, Al_2MgSi, and Al_6MgSi, the overlap of electron clouds means that covalent bonds can be confirmed between Mg-Si and Al-Si. In Fig. 8 (b1, b2, b3), electron cloud overlap is salient. It is the representative feature of covalent bonds. There is an increase in charge between Mg and Si atoms, as well as between Al and Si atoms, leading to the formation of covalent bonds. In comparison, the covalent bond in Al_6MgSi is stronger than others.

The bonding characteristic among different atoms can clearly define the mechanical property at the region of interfaces. Hence, at the interface electronic structures need to be explored entirely. Mulliken population and methods of charge density difference can concisely describe the electronic structures at Al(010)/MgSi(010), Al(010)/Al_2MgSi(001), and Al(010)/Al_6MgSi(001) interface.

The charge density differences and charge density of the Al(010)/MgSi(010), Al(010)/Al_2MgSi(001), and Al(010)/Al_6MgSi(001) interfaces are shown in Fig. 9. Although some atoms cannot be cut into the slice, we have indicated them in the figure with words to consider their effect. In Fig. 9 a, b, and c, the overlapping electron cloud at the interface means metallic bonding properties [27]. At the zone between Al and Si atoms of the Al(010)/MgSi(010) interface, the charge density is much higher than others. It reveals that there is more interaction and diffusion at the Al(010)/Al_2MgSi(001) interface. So, its binding strength is much higher. In Fig. 9 d – f, the Si, Al, and Mg atoms all lose electrons. It is the obvious trait of covalent bonding. The Si atoms at the Al(010)/MgSi(010) interface are different from those at the non-interface [28]. That can be attributed to that the Si atoms are influenced by Al atoms at the interfacial zone. It means the covalent build-up of Al-Si at the Al(010)/MgSi(010) interfaces has a stronger covalent bond at the interface.

Table 3 shows the Mulliken populations at different interfaces. At all interfaces, Al and Si atoms lost electrons. The number of electrons that come from Al and Si atoms at the Al(010)/MgSi(010) interface is 0.09 *e* and 0.11 *e*, which is higher than the other two interfaces. In addition, the band population value between interfacial

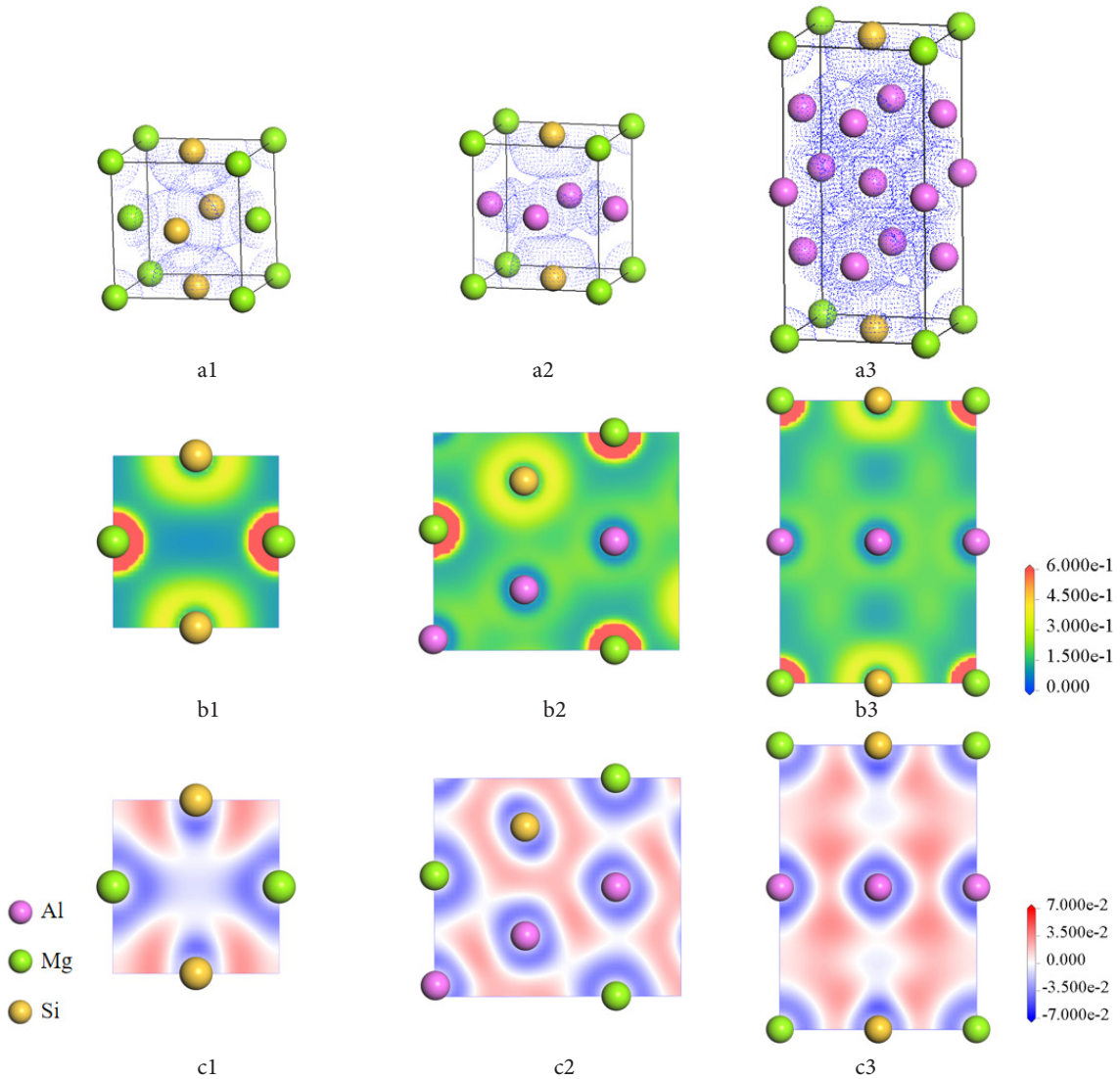

Fig. 8. (Color online) The space charge densities of MgSi (a1), Al_2MgSi (a2), and Al_6MgSi (a3) crystals, charge densities of MgSi (b1), Al_2MgSi (b2), and Al_6MgSi (b3) crystals, charge density differences for MgSi (c1), Al_2MgSi (c2), and Al_6MgSi (c3) crystals.

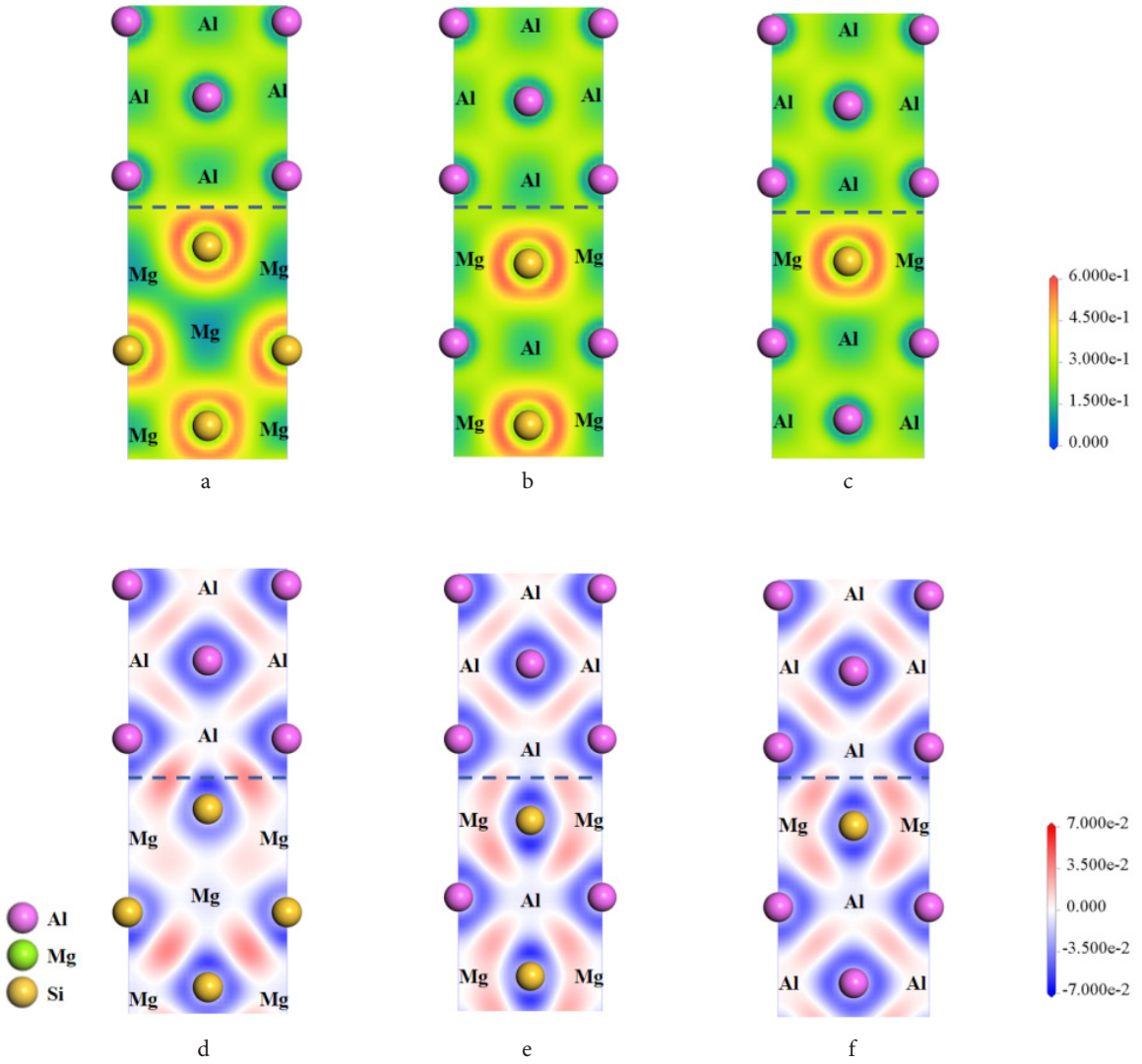

Fig. 9. (Color online) Charge density (a) and charge density difference (d) of the Al(010)/MgSi(010) interface, charge density (b) and charge density difference (e) of the Al(010)/Al_2MgSi(001) interface, charge density (c) and charge density difference (f) of the Al(010)/Al_6MgSi(001) interface (f).

Table 3. Mulliken charges at various interfaces.

	Atoms	*s*	*p*	*d*	*f*	Total	Charge (*e*)	Population
Al(010)/MgSi(010) interface	$Al_{interface}$	1.13	1.82	0	0	2.95	0.05	0.39
	Al_{bulk}	1.14	1.87	0	0	3.01	−0.01	-
	$Mg_{interface}$	2.63	7.10	0	0	9.74	0.26	-
	Mg_{bulk}	2.64	7.08	0	0	9.72	0.28	-
	$Si_{interface}$	1.58	2.72	0	0	4.30	−0.30	0.39
	Si_{bulk}	1.58	2.72	0	0	4.30	−0.30	-
Al(010)/Al_2MgSi(001) interface	$Al_{interface}$	1.13	1.85	0	0	2.98	0.02	−0.10
	Al_{bulk}	1.10	1.92	0	0	3.02	−0.02	-
	$Mg_{interface}$	2.58	7.25	0	0	9.83	0.17	-
	$Si_{interface}$	1.54	2.70	0	0	4.24	−0.24	−0.10
Al(010)/Al_6MgSi(001) interface	$Al_{interface}$	1.13	1.85	0	0	2.98	0.02	0.04
	Al_{bulk}	1.12	1.91	0	0	3.03	−0.03	-
	$Mg_{interface}$	2.59	7.26	0	0	9.85	0.15	-
	$Si_{interface}$	1.54	2.68	0	0	4.22	−0.22	0.04

Al and Si atoms is also shown in the table. Among these populations, the absolute value of the band population in the Al(010)/MgSi(010) interface is maximal. The non-zero bond population means that the bond exhibits covalent bond properties. Higher absolute value of population means the covalent bond properties are more obvious. Therefore, the Al(010)/MgSi(010) interface shows stronger covalent bond properties. The results can correspond to the charge density differences. Thus, the Al-Si covalent bond is more apparent at Al(010)/MgSi(010) interface.

3.2.3. Work function

The difference in volta potential (U_M^G) between the Al matrix and the GP zones can be described by Eq. 4 [29, 30].

$$U_M^G = (\phi^G - \phi^M)/e, \quad (4)$$

where ϕ^G and ϕ^M mean work functions of the GP zones and the Al matrix; e stands for the charge of electron.

The work function can be calculated by the following formula:

$$\phi = E_v - E_f \quad (5)$$

where E_v stands for Vacuum level, and E_f refers to Fermi energy. Their values are calculated by the CASTEP code.

Table 4 presents the calculated work functions for the Al(111), MgSi(010), $Al_2MgSi(111)$ and $Al_6MgSi(010)$ surfaces. Its values range from 4.36 eV (Al(111) surface adsorbed Cl) to 4.672 eV on the (Al(111) surface adsorbed O). Similarly, the GP zones display work functions between 4.183 eV (MgSi(010) surface adsorbed O) and 4.762 eV ($Al_6MgSi(010)$ surface adsorbed Cl). The calculated results exhibit only a narrow variance. Under atmospheric or aqueous environments, the work functions of the GP zone closely resemble those of the Al matrix. Based on Eq. (4), an average Volta potential difference of about −120 to 10 mV occurs between the Al matrix and the GP zones. This relatively small potential difference suggests a low driving force for micro-galvanic corrosion between the matrix and the precipitates, thereby contributing to the improved corrosion resistance of the material under atmospheric or aqueous environments.

Table 4. Work function of Al(111), MgSi(010), $Al_2MgSi(111)$, and $Al_6MgSi(010)$ adsorbed O/Cl.

		Fermi	Vacuum	Function
Al(111)	Al-O	−0.491	4.181	4.672
	Al-Cl	−0.172	4.188	4.36
MgSi(010)	Mg-O	0.745	4.965	4.22
	Si-O	0.788	4.971	4.183
	Mg-Cl	0.551	5.147	4.596
	Si-Cl	0.606	5.195	4.589
$Al_2MgSi(111)$	Al-O	0.246	4.714	4.468
	Si-O	0.075	4.64	4.565
	Mg-O	0.197	4.607	4.41
	Al-Cl	0.001	4.248	4.247
	Si-Cl	−0.07	4.26	4.33
	Mg-Cl	0.228	4.671	4.443
$Al_6MgSi(010)$	Al-O	0.003	4.265	4.262
	Si-O	0.544	5.139	4.595
	Mg-O	0.043	4.275	4.232
	Al-Cl	−0.056	4.637	4.693
	Si-Cl	0.587	5.223	4.636
	Mg-Cl	−0.471	4.291	4.762

3.3. Mechanical properties

Figure 10 and Table 5 present the stress-strain behavior of the sheet across different aging durations, indicating notable improvements in tensile properties with natural aging. Specifically, the ultimate tensile strength rises from 185 MPa at 0 days to 215 MPa at 28 days, marking a 16.2% (30 MPa) increase. Similarly, the yield strength shows a substantial gain, climbing from 59.3 MPa at 0 days to 91 MPa after 21 days of aging — a 53.5% (31.7 MPa) enhancement. These results suggest that natural aging positively impacts the strength of the alloy.

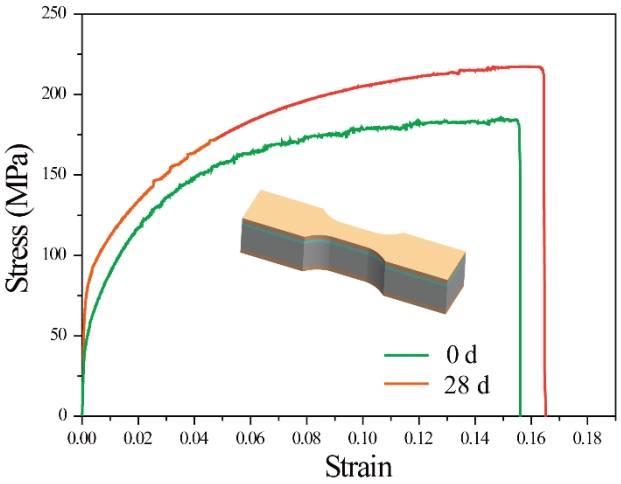

Fig. 10. (Color online) Stress-strain curves for the sheet with various aging processes.

Table 5. Multi-layered Al sheet mechanical properties after natural ageing.

Time(h)	Mechanical properties	
	YS (MPa)	UTS (MPa)
0	59.3 ± 4.6	185 ± 5.5
504	91 ± 6.2	215 ± 6.4

3.4. Corrosion

The localized corrosion on the Al sheet surface initiates corrosion attack along grain boundaries, reaching into the core material and exposing it further to corrosive environments. This process is exacerbated by a galvanic coupling that forms between the Al matrix and grain boundaries. SEM results of the Al sheet surface before and after SWAAT are shown in Fig. 11. It reveals that α-Al(Fe, Mn)Si particles act as local cathodes relative to the Al matrix, accelerating the dissolution of the matrix in exposed areas [8–10]. Pitting begins at the α-Al(Fe, Mn)Si/Al matrix interface and quickly spreads into the matrix, which is still far from a second-phase particle. Eventually, while the Al matrix exhibits extensive corrosion, the α-Al(Fe, Mn)Si particles remain relatively intact.

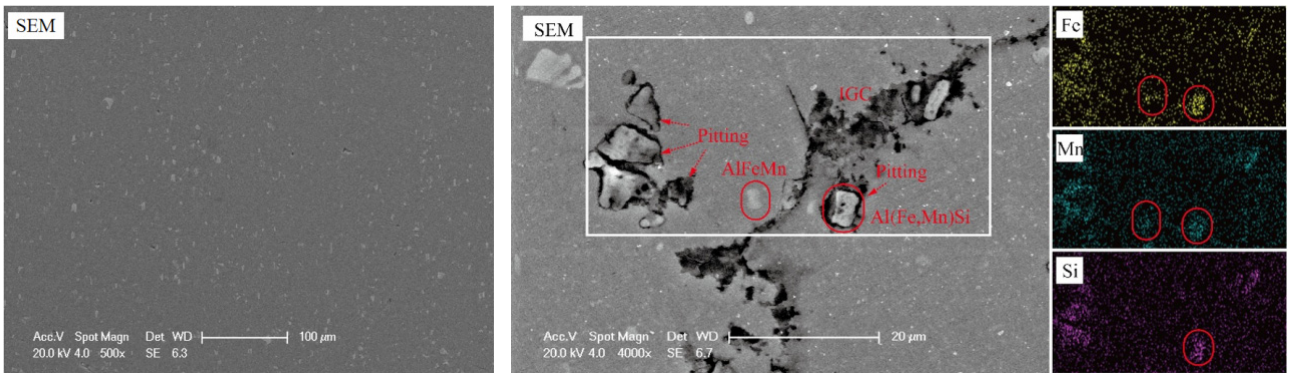

a b

Fig. 11. (Color online) SEM results of the sheet before SWAAT (a), and after SWAAT (b).

4. Discussion

4.1. Enhancement of the mechanical properties with natural aging

Natural aging process significantly enhances the mechanical properties of an Al alloy by inducing microstructural changes. Zhao's model [31] for the yield strength (σ_y) in Al alloys can be applied as follows:

$$\sigma_y = \sigma_{gb} + M_A(\tau_0 + \Delta\tau_s + (\Delta\tau_d^2 + \Delta\tau_p^2)^{1/2}) \quad (6)$$

The critical resolved shear stress of pure Al, denoted as τ_0, is approximately 10 MPa, while σ_{gb} refers to strengthening at the grain boundaries, and M_A indicates the average Taylor factor. The solid solution strengthening, denoted by $\Delta\tau_s$, is influenced by solute types and concentrations, $\Delta\tau_d$ relates to dislocation strengthening, affected by dislocation density. Additionally, $\Delta\tau_p$ denotes precipitation strengthening, contingent on dispersoid type, size, and density [32]. Of these, precipitation strengthening plays a critical role in aging reinforcement.

In the work, a core layer with high strength was exploited, with TEM images (Fig. 12) revealing dispersoid morphology essential for strengthening. Conversely, brazed samples exhibited fewer precipitates, resulting in a yield strength (59.3 MPa), as shown in Fig. 10.

After 28 days of natural aging, the core layer achieves the yield strength of 91 MPa (Fig. 10), which underscores the significant impact of aging on alloy performance. The principal strengthening mechanism during natural aging lies in the formation of nano-precipitated phases with a high density. Figure 13a shows the phases containing numerous needle-shaped precipitates, which are observed by the $<011>_{Al}$ zone axis diffraction patterns. This structure is crucial for enhancing the mechanical properties, as confirmed by TEM imaging. Figure 13b enlarges part of the precipitate structures, while FFT analysis (Fig. 13c) reveals no additional diffraction spots, indicating that these precipitates share crystal structure the same as Al matrix, which maintains full coherence with the matrix. Using HRTEM, further insight into the needle-shaped and short lath-shaped precipitates is provided (Fig. 13d). The inverted FFT image of the (111)Al plane (Fig. 13e) shows an interplanar spacing of 0.204 nm, with Fig. 13f mapping a marked segregation of Mg and Si within the matrix. Critically, these precipitates are consistent with GP zones [33], which, as demonstrated in research of Murayama [34], are entirely consistent with the matrix. This observation is consistent with calculations indicating stronger covalent bonding at the Al/MgSi interface. Specifically, the MgSi precipitate phase more readily bonds with the interface, resulting in higher work of adhesion and promoting the formation of additional MgSi precipitates.

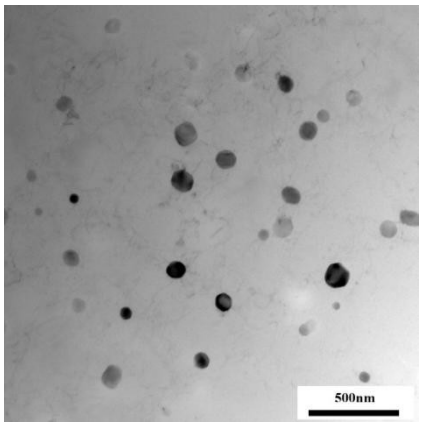

Fig. 12. Precipitates in TEM bright field image for brazed samples.

The precipitation sequence within Al-Fe-Mn-Si-Mg alloys as outlined by key studies [35] can be illustrated as:

supersaturated solid solution →
→ clusters and GP zones → β'' → β' → β

This sequence progresses from clusters to GP zones and β'' phases, with clusters appearing as aggregates within the Al matrix [33, 36]. In this alloy system, clusters generally exhibit a spherical shape, while GP zones adopt either a needle or spherical form [37]. The current study identifies GP zones in a needle-like morphology, suggesting that precipitation of β'' are largely inhibited during aging.

Effectiveness of these precipitates can be partly attributed to differences in the shear modulus and size of atom between the solutes (Si and Mg) and the Al matrix. For instance, in Al solid solution, Mg atom radius is more than 12% larger compared to Al atoms, while Si atoms are about 5% smaller [38]. This discrepancy causes elastic deformation at the GP zones-Al matrix interface, despite their full coherency. Localized strain fields form due to the atomic mismatch

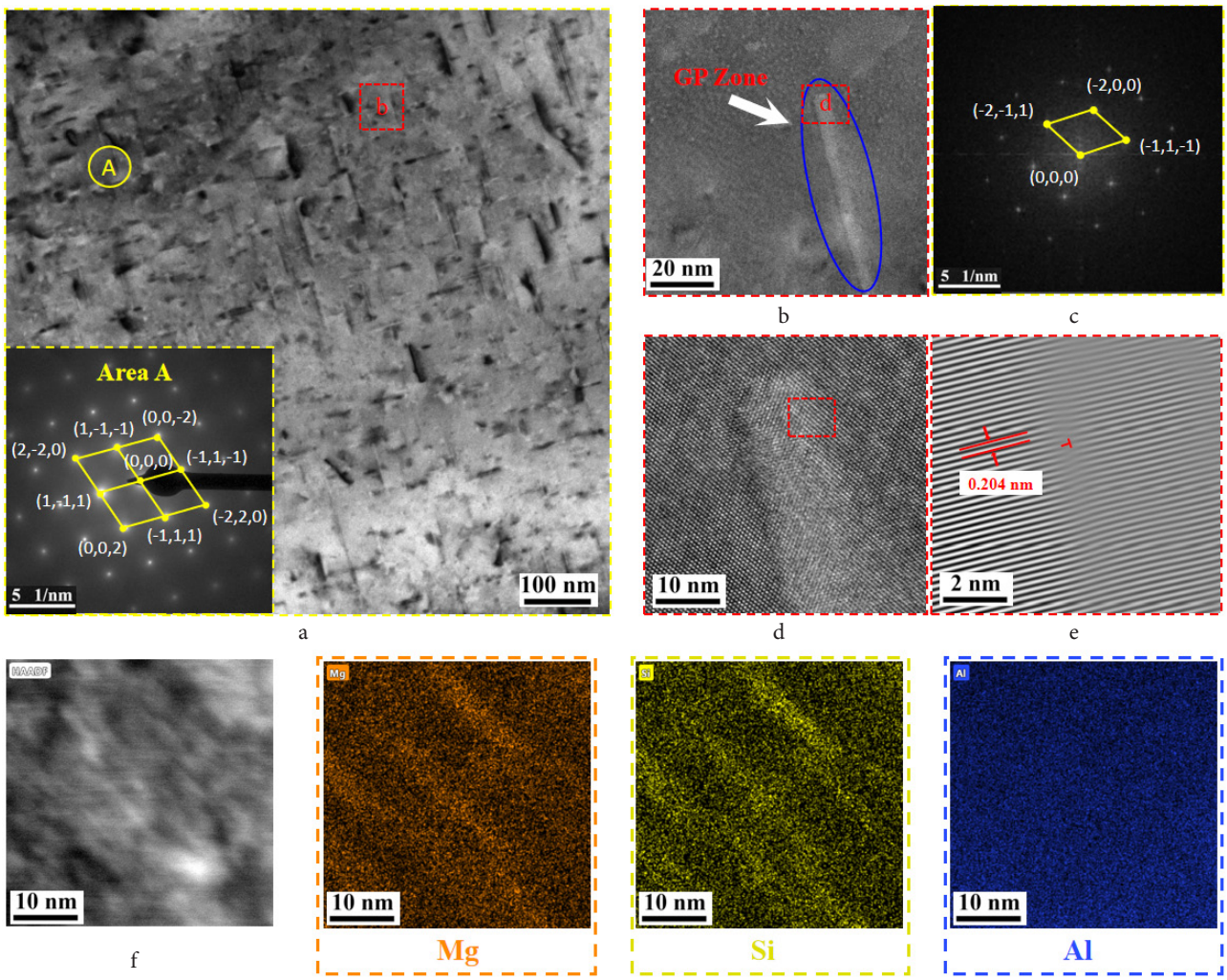

Fig. 13. (Color online) After the natural aging treatment, the precipitates in the TEM image. The TEM bright-field image and corresponding SAED in the area A (a); enlarged image marked in Fig. 13 a (b); the corresponding FFT (c); enlarged image from Fig. 13 b (d); the inverted FFT of selected (111)Al reflection (e); mapping for the needle-shaped precipitations (f). Misfit dislocation is marked as "⊥".

between Mg, Si, and Al, which in turn restricts dislocation movement through the lattice [39]. This dislocation-blocking mechanism plays a significant role in enhancing the yield strength of the alloy.

4.2. Corrosion mechanism

Preliminary calculations demonstrate that Al particles have an average work function of 4.08 eV. However, the work function of α-Al(Fe, Mn)Si particles distributed in the range of 4.22 – 4.29 eV across different surfaces [29]. The Volta potential difference between the Al matrix and α-Al(Fe, Mn)Si particles is 170 – 220 mV. The Volta potential of α-Al(Fe, Mn)Si particles is positive compared to the Al matrix. Hence, these particles behave as cathodic phases, which accelerates Al matrix dissolution process. When areas of exposed α-Al(Fe, Mn)Si particles are in contact with the Al matrix, the matrix around these particles corrodes preferentially, initiating pitting at the particle-matrix interface. Over time, corrosion rapidly extends into the matrix, leaving the α-Al(Fe, Mn)Si particles relatively intact while the surrounding Al matrix undergoes significant degradation, as shown in Fig. 11.

Further calculations findings reveal the GP zones exhibit work functions between 4.183 eV and 4.762 eV, yielding a much smaller Volta potential difference of −120 to 10 mV relative to the Al matrix. This similarity in potential between the matrix and the GP zones inhibits the galvanic corrosion process typically initiated by potential differences. As a result, no pitting corrosion is observed around the GP zones, which aligns with theoretical predictions.

5. Conclusions

Calculations and microstructural studies of the AA4343/AA3xxx/AA3xxx/AA4343 layered alloys highlight the presence of an interlayer as a diffusion barrier layer, particularly restricting movement of Si from the clad to the core layer during brazing process. This interlayer enables these alloys to achieve an optimal combination of corrosion resistance and mechanical strength, a property that supports their use in automotive heat exchangers.

1. Interlayer effectively limits Si diffusion, confining it within the clad layer and enhancing the microstructural stability of the core layer.

2. With various stacking modes, the maximum of W_{ad} can be achieved at the type of B-C among the Al(010)/MgSi(010) interfaces. It can reach 1.52 J/m^2. For the Al(010)/Al_2MgSi(001) interface, the maximal value of W_{ad} is 1.15 J/m^2. At the Al(010)/Al_6MgSi(001) interface, W_{ad} is 1.24 J/m^2. The d_0 of these interfaces is 2.4, 2.2, and 2.2 Å, respectively. Metallic and covalent bonds between Si and Al atoms at the Al(010)/MgSi(010) interface are more obvious than others at other interfaces. As a result, there are more MgSi crystals that are retained by these bonds in the GP zones.

3. Computational predictions indicate that adsorbed work functions for particles like MgSi, Al_2MgSi, and Al_6MgSi exhibit a much smaller Volta potential compared to the Al matrix. This small potential difference reduces galvanic activity between surrounding matrix and GP particles, resulting in limited corrosion effects on the GP zones.

4. With natural aging, the Mg and Si appear in the core layer promoting the formation of the GP zone and contributing significantly to the tensile strength of the alloy. After 28 days of aging, the ultimate tensile strength of the alloy could reach 215 MPa, representing a 16.2% increase.

Declaration of competing interest: *The authors declare that they have no known competing financial interests or personal relationships that could have appeared to influence the work reported in this paper.*

References

1. Z. H. Jiang, Y. Zhuang, Y. Li, S. J. Li, Effect of Modification Treatment on Inclusions in 430 Stainless Steel by Mg-Al Alloys, J. Iron. Steel Res. Int. 20 (2013) 6–10.
2. Z. Yuan, J. Chang, Y. Tu, T. Yuan, C. Liu, L. Huang, Z. Ni, X. Wang, J. Peng, Z. Ling, J. Shi, P. He, Metallurgical interactions in solid/liquid diffusion couples of AA4343/AA3xxx/AA4343 layered aluminum sheet, J. Mater. Res. Technol. 28 (2024) 1633–1643.
3. Y. J. Shi, L. J. Liu, L. Zhang, L. J. Zhang, L. Zheng, R. X. Li, B. Y. Yu, Effect of squeeze casting process on microstructures and flow stress behavior of Al-17.5Si-4Cu-0.5Mg alloy, J. Iron. Steel Res. Int. 24 (2017) 957–965.
4. H. C. Li, M. Li, D. Y. Yang, F. Y. Cao, Y. D. Jia, Z. S. Yu, J. Zhao, T. Liu, H. Zhan, Q. Chen, J. F. Sun, Aging behavior and precipitate characterization of Zn-rich Al-Zn-Mg-Cu alloys with various Mg and Cu contents, J. Mater. Res. Technol. 28 (2021) 1064–1073.
5. H. Jin, M. S. Kozdras, B. S. Amirkhiz, S. L. Winkler, Liquid–Solid Interaction in Al-Si/Al-Mn-Cu-Mg Brazing Sheets and Its Effects on Mechanical Properties, Metall. Mater. Trans. A. 49 (2018) 3091–3107.
6. D. J. Schmatz, Grain-Boundary Penetration during Brazing of Aluminum, Weld. J. 62 (1983) S267–S271.
7. S. Wang, K. Luo, S. Tao, G. Li, J. Cui, Corrosion behavior and failure mechanism of electromagnetic pulse welded joints between galvanized steel and aluminum alloy sheets, J. Manuf. Process. 64 (2021) 937–947.
8. F. N. Afshar, R. Ambat, C. Kwakernaak, J. H. W. De Wit, J. M. C. Mol, H. Terryn, Electrochemical depth profiling of multilayer metallic structures: an aluminum brazing sheet, Electrochim. Acta. 77 (2012) 285–293.
9. F. N. Afshar, F. D. Tichelaar, A. M. Glenn, P. Taheri, M. Sababi, H. Terryn, J. M. C. Mol, Improved corrosion resistance of aluminum brazing sheet by a post-brazing heat treatment, Corrosion. 73 (2017) 379–393.
10. F. N. Afshar, J. H. W. De Wit, H. Terryn, J. M. C. Mol, Scanning Kelvin probe force microscopy as a means of predicting the electrochemical characteristics of the surface of a modified AA4xxx/AA3xxx (Al alloys) brazing sheet, Electrochim. Acta. 88 (2013) 330–339.
11. Z. Yuan, Y. Jiang, Y. Lu, K. Zhang, H. Xie, Z. Ni, L. Huang, J. Liu, X. Wang, J. Peng, Z. Ling, J. Shi, P. He, Enhancing corrosion resistance of Al alloy sheets with potential gradient by arc-sprayed Zn coatings, J. Mater. Res. Technol. 33 (2024) 6263–6274.
12. Q. Shi, F. Liang, B. Cheadle, Electrochemical behaviors of quad-layer aluminum brazing sheet composite for automotive applications, Corrosion 60 (2004) 492–500.
13. W. Kohn, L. J. Sham, Self-consistent equations including exchange and correlation effects, Phys. Rev. 140 (1965) A1133.
14. G. Kresse, J. Furthmüller. Efficient iterative schemes for *ab initio* total-energy calculations using a plane-wave basis set, Phys. Rev. B. 54 (1996) 11169.
15. J. P. Perdew, K. Burke, M. Ernzerhof, Generalized gradient approximation made simple, Phys. Rev. lett. 77 (1996) 3865.
16. P. E. Blöchl, Projector augmented-wave method, Phys. Rev. B. 50 (1994) 17953.
17. C. Ravi, C. Wolverton, First-principles study of crystal structure and stability of Al-Mg-Si-(Cu) precipitates, Acta Mater. 52 (2004) 4213–4227.
18. F. Liu, F. Guo, H. Chen, Y. Ouyang, X. Tao, Y. Feng, Y. Du, Elastic constants and thermophysical properties of Al-Mg-Si alloys from first-principles calculations, Paper presented at the 2nd Sino-German Symposium on Computational Thermodynamics and Kinetics and their Applications to Solidification. 101 (2010) 1392–1397.
19. K. Matsuda, S. Ikeno, H. Gamada, K. Fujii, Y. Uetani, T. Sato, A. Kamio, High-resolution electron microscopy on the structure of Guinier-Preston zones in an Al-1.6 mass Pct Mg_2Si alloy, Metall. Mater. Trans. A. 29 (1998) 1161–1167.
20. A. Standard, E8/E8M-16a standard test methods for tension testing of metallic materials, West Conshohocken: ASTM Int. (2016).
21. F. N. Afshar, E. Szala, A. Wittebrood, R. Mulder, J. M. C. Mol, H. Terryn, J.H.W. de Wit, Influence of material related parameters in sea water acidified accelerated test, reliability analysis and electrochemical evaluation of the test for aluminum brazing sheet, Corros. Sci. 53 (2011) 3923–3933.
22. Z. Yuan, Y. Tu, H. He, T. Yuan, Q. Zhang, X. Peng, Influence of final annealing temperature on the microstructural evolution and corrosion resistance of a Sandwich multi-layered aluminum sheet, Mater. Res. Express. 6 (2018) 026536.
23. D. Y. Dang, L. Y. Shi, J. L. Fan, H. R. Gong, First-principles study of W-TiC interface cohesion, Surf. Coat. Tech. 276 (2015) 602–605.

24. Z. Liu, A. Wang, P. Liu, J. Xie, The effect mechanism of Zn, Ni and Mn solute elements on the WC/Cu-based filler metal interfacial properties: first-principles calculations and experiments, J. Mater. Res. Technol. 18 (2022) 2354 – 2362.
25. J. Yang, W. Wei, J. Liu, L. Zhang, C. Ye, X. Song, J. Feng, Understanding the interfacial properties in BN-SiO_2 diphase ceramic/TiNiNb filler alloy systems: First-principles and mechanical studies, Appl. Surf. Sci. 556 (2021) 149563.
26. X. Wang, G. Wu, S. Li, P. He, N. Fang, W. Long, Effect of N-Cr compounds on the brazing of high nitrogen steel with Ag-based filler metal: first-principles calculation, J. Mater. Res. Technol. 23 (2023) 370 – 378.
27. Y. Lu, X. Wang, J. Shi, K. Pan, L. Zhang, Y. Peng, X. Chen, Y. Zhang, Multiscale consideration of mechanism revealing in diamond brazing with a novel NiTiZrCrVAl amorphous filler alloy: First-principles and experimental perspective, J. Mater. Res. Technol. 23 (2025) 3811 – 3824.
28. X. Fan, B. Chen, M. Zhang, D. Li, Z. Liu, C. Xiao, First-principles calculations on bonding characteristic and electronic property of TiC(111)/TiN(111) interface, Mater. Des. 112 (2016) 202 – 289.
29. Z. Yuan, Y. Tu, T. Yuan, Y. Huang, Y. Zhang, Gradient multilayer aluminium sheets used in automotive heat exchangers, J. Mater. Sci. 56 (2021) 5215 – 5232.
30. Z. Yuan, Y. Tu, T. Yuan, Z. Ni, X. Chen, C. Liu, Designing structures with combined gradient of potential and precipitation in multi-layered aluminum sheet for simultaneous improvement of mechanical properties and corrosion resistance, J. of Manuf. Process. 97 (2023) 159 –170.
31. J. Zhao, Z. Liu, S. Bai, D. Zeng, J. Wang, Effects of natural aging on the formation and strengthening effect of G.P. zones in a retrogression and re-aged Al-Zn-Mg-Cu alloy, J. Alloys Compd. 829 (2020) 154469.
32. X. B. Yang, J. H. Chen, J. Z. Liu, F. Qin, J. Xie, C. L. Wu, A high-strength AlZnMg alloy hardened by the T-phase precipitates, J. Alloys Compd. 610 (2014) 69 – 73.
33. C. D. Marioara, S. J. Andersen, J. Jansen, H. W. Zandbergen, Atomic model for GP-zones in a 6082 Al-Mg-Si system, Acta Mater. 49 (2001) 321 – 328.
34. M. Murayama, K. Hono, Pre-precipitate clusters and precipitation processes in Al-Mg-Si alloys, Acta Mater. 47 (1999) 1537 –1548.
35. X. Wang, S. Esmaeili, D. J. Lloyd, The sequence of precipitation in the Al-Mg-Si-Cu alloy AA6111, Metall. Mater. Trans. A. 37 (2006) 2691 – 2699.
36. H. S. Hasting, J. C. Walmsley, A. T. J. Van Helvoort, C. D. Marioara, S. J. Andersen, R. Holmestad, Z-contrast imaging of the arrangement of Cu in precipitates in 6XXX-series aluminium alloys, Philo. Mag. Lett. 86 (2006) 589 – 597.
37. K. Matsuda, S. Ikeno, H. Matsui, T. Sato, K. Terayama, Y. Uetani, Comparison of precipitates between excess Si-type and balanced-type Al-Mg-Si alloys during continuous heating, Metall. Mater. Trans. A. 36 (2005) 2007 – 2012.
38. S. Esmaeili, X. Wang, D. J. Lloyd, W. J. Poole, On the precipitation-hardening behavior of the Al-Mg-Si-Cu alloy AA6111, Metall. Mater. Trans. A. 34 (2003) 751 – 763.
39. C. Varvenne, G. P. M. Leyson, M. Ghazisaeidi, W. A. Curtin, Solute strengthening in random alloys, Acta Mater. 124 (2017) 660 – 683.